

## Power balance in a high-density field reversed configuration plasma

R. M. Renneke,<sup>1,a)</sup> T. P. Intrator,<sup>1</sup> S. C. Hsu,<sup>1</sup> G. A. Wurden,<sup>1</sup> W. J. Wagenaar,<sup>1</sup>  
E. L. Ruden,<sup>2</sup> and T. C. Grabowski<sup>2</sup>

<sup>1</sup>Los Alamos National Laboratory, M.S. E526, Los Alamos, New Mexico 87545, USA

<sup>2</sup>Air Force Research Laboratory, Kirtland Air Force Base, Albuquerque, New Mexico 87117, USA

(Received 15 February 2008; accepted 22 April 2008; published online 5 June 2008)

A global power balance analysis has been performed for the Field Reversed Experiment with Liner high density ( $>5 \times 10^{22} \text{ m}^{-3}$ ) field reversed configuration (FRC) plasma. The analysis was based on a zero-dimensional power balance model [D. J. Rey and M. Tuszewski, *Phys. Fluids* **27**, 1514 (1984)]. The key findings are as follows. First, the percentage of radiative losses relative to total loss is an order of magnitude lower than previous lower density FRC experiments. Second, Ohmic heating was found to correlate with the poloidal flux trapping at FRC formation, suggesting that poloidal flux dissipation is primarily responsible for plasma heating. Third, high density FRCs analyzed in this work reinforce the low-density adiabatic scaling, which shows that particle confinement time and flux confinement time are approximately equal. © 2008 American Institute of Physics. [DOI: 10.1063/1.2934588]

### I. INTRODUCTION

High-density ( $\sim 10^{17} \text{ cm}^{-3}$ ) field-reversed configuration (FRC) plasmas are being studied as the magnetized target for magnetized target fusion (MTF),<sup>1</sup> which is an approach to fusion intermediate in density between magnetic and inertial fusion. MTF is a subset of magneto-inertial fusion (MIF), which is based on the idea of adiabatically compressing a magnetized target plasma to fusion conditions using an imploding “pusher.” In our case, we will implode a metal liner onto a FRC.

The Field-Reversed Experiment-Liner (FRX-L) at Los Alamos National Laboratory has successfully formed FRCs with  $5 \times 10^{16} \text{ cm}^{-3}$  electron density and  $\sim 300 \text{ eV}$  total temperature, suitable for MTF experiments at the Air Force Research Laboratory, Kirtland Air Force Base (AFRL-Kirtland) to be carried out over the next few years.<sup>2,3</sup> FRX-L has two primary goals: first, to create a stationary FRC and optimize/characterize it; and second, to translate this FRC from a formation chamber to a compression chamber. Demonstrated technology<sup>3</sup> for radial implosion mandates a certain threshold for density and temperature after the translation. The confinement time must also exceed the FRC transit time from the formation to implosion chambers. The status of present technology indicates that a FRC with density  $\sim 1 \times 10^{17} \text{ cm}^{-3}$ , total temperature  $300 \text{ eV}$ , and confinement time  $10\text{--}20 \mu\text{s}$  is necessary.

In order to optimize the FRC for compression, it is useful to quantify losses from various sources. A global power balance model pioneered by Rey and Tuszewski<sup>4</sup> and modified by Maqueda<sup>5</sup> is used here. All quantities needed are either measured routinely on FRCs or can be easily inferred from the data. This model assumes that the only losses for a FRC are through thermal conduction, particle cross-field diffusion, and radiation.

For most plasma devices, attainment of a hot

( $T > 200 \text{ eV}$ ) plasma is hindered by radiation barriers from impurities.<sup>6</sup> A radiation barrier forms because plasma impurities radiate energy away faster than the plasma can be heated. FRX-L largely avoids this problem by using a theta pinch with ringing PI formation technique,<sup>7</sup> which quickly heats the plasma past the radiation barrier. However, there is a concern that impurities in the plasma will degrade performance during the FRC equilibrium phase. Plasma impurities are a common occurrence in FRC plasmas<sup>8</sup> and sometimes require extensive mitigation.<sup>9</sup> For this work, we focused our efforts on quantifying the radiative loss from a high-density FRC and not on impurity mitigation.

### II. EXPERIMENTAL SETUP AND DIAGNOSTICS

FRX-L forms high-density ( $1 \times 10^{16} \text{ cm}^{-3}$ ) FRCs using the field-reversed theta pinch (FRTP) method.<sup>10</sup> A schematic view of the experimental setup is shown in Fig. 1. The coil is a single-turn theta pinch broken into four axial segments to allow diagnostic access between sections. Both ends of the coil section contain cusp coils which form a magnetic null point that causes magnetic reconnection and programmed formation of the FRC. The flux excluder plates shield the cusp coils from the fast-changing magnetic flux generated by the theta coils. This reduces the mutual inductance between the theta coil and cusp coils, thus preventing induced high voltages in the cusp coils.

The FRTP technique is illustrated in Fig. 2 with a time history of the theta coil current. Details of the formation process are available in a previous paper.<sup>11</sup> The solid black and dashed red traces in Fig. 2 provide a comparison of the “old” crowbar to the “new” crowbar. The new crowbar shows much reduced field modulation, which improves FRC lifetime.

An eight-chord helium–neon interferometer is used to measure the midplane density profile. The interferometer viewing plane is shown in Fig. 1. The eight chords have radial impact parameters ranging from 0 to 4.0 cm. This

<sup>a)</sup>Electronic mail: renneke@lanl.gov.

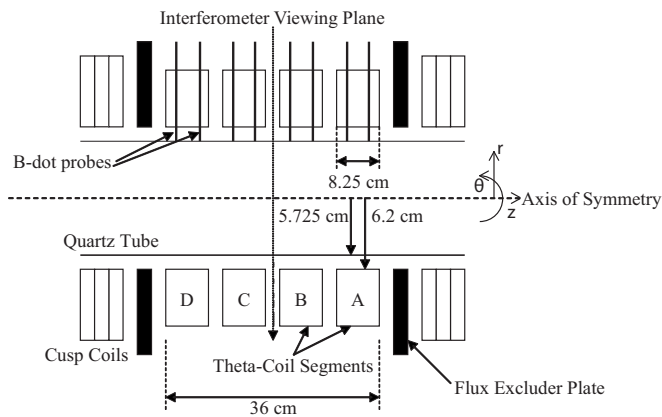


FIG. 1. FRX-L experimental setup. A top view with locations of some key diagnostics is shown.

spread covers the area of the FRC plasma and allows Abel inversion of the data, which can produce a radial density profile as a function of time.<sup>12</sup> The central chord combined with the separatrix radius at the center of the FRC yields the volume-averaged density shown in Fig. 4 below.

Radiation is determined from bolometry using a highly responsive (near theoretical quantum efficiency of 91%) photodiode array.<sup>13</sup> The bolometer responds to photons as well as electrons and protons. The response between particles and photons can be distinguished by the time-of-flight from the plasma to the detector. Typical electron temperatures in FRX-L can be estimated at 100–200 eV, so the approximate one meter distance between the plasma and detector can be traversed in 12  $\mu$ s. The typical lifetime of the plasma is 10  $\mu$ s or less, so any particle response will appear after the termination of the discharge. The bolometer was mounted at the end of the experiment as shown in Fig. 3. The axial view was chosen due to the need for vacuum access to the plasma. A benefit of the large distance between the plasma and bolometer is a reduction of the photon flux incident on the detector. Note from the figure that there are three bolometer

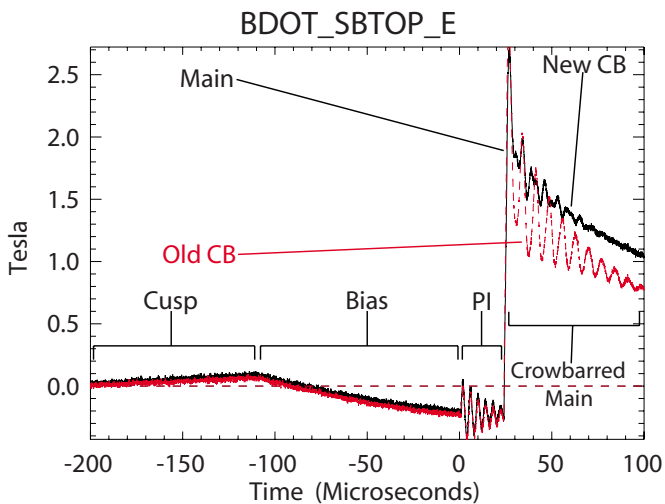


FIG. 2. (Color online) Magnetic field for  $\theta$ -coil segment B. External magnetic field modulation is improved on the new crowbar vs the old crowbar.

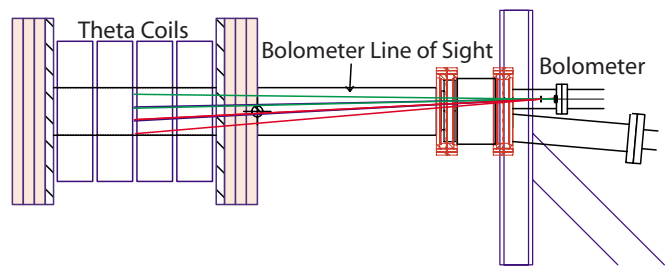


FIG. 3. (Color online) Bolometer viewing geometry. Bolometer active area is in upper tube at top right; bolometer is designed so the lines of sight for all three channels together cover the entire quartz tube cross section.

detectors which split the area of the quartz tube roughly into thirds. The signals must be added to estimate the total radiative emission of the FRC.

The radiated power can be expressed as

$$P_{\text{rad}} = \frac{P_{\text{det}}}{f_{\text{geom}}}, \quad (1)$$

where  $f_{\text{geom}}$  is a geometric factor given by

$$f_{\text{geom}} = \frac{A}{4\pi r_s^2 l_s} [\sqrt{b^- + 4r_s^2} - \sqrt{b^+ + 4r_s^2} - \sqrt{b^-} + \sqrt{b^+}] \quad (2)$$

and  $b^\pm$  is given by

$$b^\pm = 4l_A^2 \pm 4l_A l_s + l_s^2. \quad (3)$$

The distance  $l_A$  is the length from the slit window to the center of the FRC plasma.  $l_s$  and  $r_s$  are the separatrix length and radius, respectively. The bolometer can be modeled as a current source with high impedance ( $\approx 1000$  M $\Omega$ ). The termination resistance  $R$  is typically 50 ohms, and hence there is little distortion in the signal. Under these assumptions the power from the bolometer diode can be written

$$P_{\text{det}} = \sum_{i=1}^3 \frac{C_i}{RA_w}, \quad (4)$$

where  $C_i$  is the raw voltage response from each bolometer channel (3 in total). The average bolometer response  $A_w$  is 24 A/W of incident power.

Magnetic probes (“B-dots”) are available at two positions per segment of the theta coil. The magnetic probes measure the external magnetic field. Flux loops, which are not shown in Fig. 1, are distributed one per coil section. Flux loops measure the total poloidal flux present in the FRC plasma. “B-dot” probes, flux loops, and interferometry provide the plasma density, temperature, and physical dimensions. This is possible by assuming radial pressure balance and using the average beta condition for elongated FRCs,<sup>7</sup>

$$\langle \beta \rangle = 1 - \frac{x_s^2}{2}. \quad (5)$$

The bolometer provides total radiated power for the power balance model described in Sec. III. More details concerning the diagnostics and experimental measurements are available in previous FRX-L papers.<sup>2,11</sup>

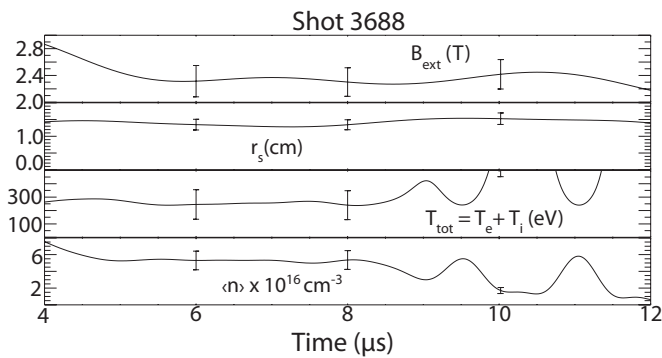


FIG. 4. FRX-L typical parameters. External magnetic field, separatrix radius, total temperature, and average density are shown. Time is measured after the main bank fires.

These diagnostics are used for characterizing the parameters  $n$ ,  $\tau$ , and  $T$  of the plasma triple product for fusion devices. Typical quantities for our FRC are shown in Fig. 4. The x-axis in Fig. 4 is the time after the main bank fires (as shown in Fig. 2). This timing is used in order to compare different shots with different relative timings between the main capacitor bank and PI bank.

### III. GLOBAL POWER BALANCE MODEL

A global power balance analysis has been performed on FRX-L to determine the relative importance of losses and to determine the plasma energy content which will affect scaling to the MTF regime. A global power balance is a volume-averaged approach that simply takes all the sources for plasma energy and balances them with losses. Rej and Tuszewski have derived the zero-dimensional case,<sup>4</sup> which will be used for FRX-L.

High density FRCs in FRX-L evolved very dynamically over the course of the shot. Shots with dynamic nonequilibrium behavior were excluded by a series of tests. These tests, detailed below, checked the volume-averaged model by comparing it with more detailed diagnostic information provided by a multichord interferometer. The interferometer yields line-averaged density for different chord paths, which can be reconstructed into a radial density profile by using tomography. Only shots and time windows which passed these tests were considered in later data analysis.

#### A. Overview of the Rej–Tuszewski model

In the single fluid model, there are two direct sources of plasma heating after the initial shock: compressional heating due to magnetic pressure present after the initial main field rise, and Ohmic heating due to magnetic flux trapped in the plasma resistively decaying away. There are three sources of power loss: radiation, primarily due to plasma impurities; conduction, mainly due to electron thermal conduction at the edge layer; and convection, due to particle cross-field diffusion. Figure 5 (adapted from Ref. 4) summarizes these inputs and outputs. The power balance is

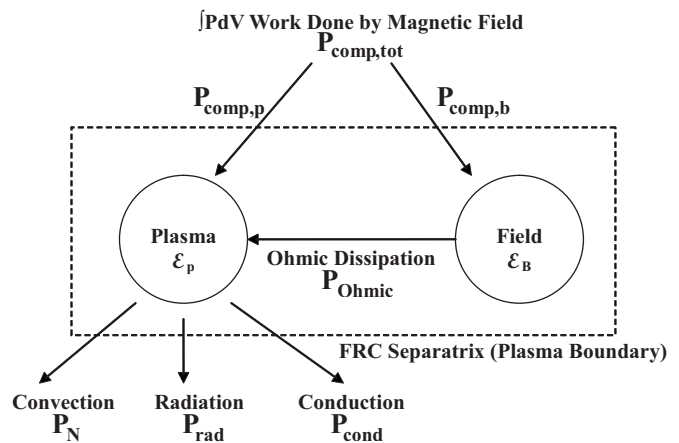


FIG. 5. Power balance diagram. Compressional work enters the FRC via the action of external magnetic fields; power leaves the FRC by radiation, conduction, and convection; and energy stored in internal magnetic fields is dissipated by Ohmic heating.

$$\frac{d\mathcal{E}_p}{dt} = P_{\text{comp},p} + P_{\text{Ohmic}} - P_N - P_{\text{rad}} - P_{\text{cond}}, \quad (6)$$

where  $\mathcal{E}_p$  is the energy present in the plasma.  $P_{\text{comp},p}$  is the plasma compression power provided by the external magnetic field.  $P_{\text{Ohmic}}$  is the Ohmic heating, and  $P_N$ ,  $P_{\text{rad}}$ , and  $P_{\text{cond}}$  represent power loss by convection, radiation, and conduction, respectively. The Ohmic heating is related to compressional work done on the magnetic field in the following manner:

$$\frac{d\mathcal{E}_B}{dt} = P_{\text{comp},b} - P_{\text{Ohmic}}, \quad (7)$$

where  $\mathcal{E}_B$  is energy stored in magnetic fields. Assuming that  $l_s \gg 2r_s$ , i.e., an elongated FRC, and that the FRC is approximately cylindrical (neglecting end effects) it can be shown for the adiabatic case,<sup>7,14</sup>

$$\mathcal{E}_p = \frac{3}{2} \left( \frac{B_{\text{ext}}^2}{2\mu_0} \right) V_{\text{FRC}} \left( 1 - \frac{x_s^2}{2} \right),$$

$$\mathcal{E}_B = \frac{3}{2} \left( \frac{B_{\text{ext}}^2}{2\mu_0} \right) V_{\text{FRC}} \left( \frac{x_s^2}{2} \right),$$

$$P_{\text{comp,tot}} = \frac{dW}{dt} = -P_m V \left( \frac{2}{x_s} \frac{dx_s}{dt} + \frac{1-x_s^2}{l_s} \frac{dl_s}{dt} \right), \quad (8)$$

$$P_{\text{comp},b} = \mathcal{E}_B \left( \frac{2}{B_{\text{ext}}} \frac{dB_{\text{ext}}}{dt} + \frac{1}{V} \frac{dV}{dt} + \frac{2}{x_s} \frac{dx_s}{dt} \right),$$

$$P_{\text{comp},p} = -\frac{2}{3} \mathcal{E}_p \left( \frac{1}{V} \frac{dV}{dt} \right) + \frac{\mathcal{E}_B}{2x_s} \frac{dx_s}{dt}.$$

Refer to Fig. 5 for the relationship between these quantities. The constant 3/2 present in the equations for  $\mathcal{E}_p$  and  $\mathcal{E}_B$  is a result of assuming a Maxwellian distribution and an ideal monatomic gas for the deuterium plasma.

These equations are valid only in the limiting case that no Ohmic heating occurs and there are no losses from the

plasma ( $P_{\text{Ohmic}}=0$ ,  $P_{\text{loss}}=P_N+P_{\text{rad}}+P_{\text{cond}}=0$ ). These quantities are finite and will introduce error into the energy balance. The volume-averaged model assumes that Eqs. (8) are valid even when  $P_{\text{Ohmic}}$  and  $P_{\text{loss}}$  are nonzero, i.e., for small perturbations of  $P_{\text{Ohmic}}$  and  $P_{\text{loss}}$ . These quantities are considered as a perturbation on the adiabatic case. For the perturbed case we can write

$$P_{\text{Ohmic}} = -\mathcal{E}_B \left( \frac{13}{2x_s} \frac{dx_s}{dt} + \frac{2}{B_{\text{ext}}} \frac{dB_{\text{ext}}}{dt} \right),$$

$$P_N = \frac{5N_e T}{2\tau_N}, \quad (9)$$

$$P_{\text{cond}} = P_{\text{comp},p} + P_{\text{Ohmic}} - P_N - P_{\text{rad}} - \frac{d\mathcal{E}_p}{dt}.$$

## B. Application of power balance model to FRX-L

It is important to note that this model imposes many constraints on the analyzed FRC and may not be suitable for all FRCs. Checking the FRC behavior is prudent before attempting to apply the model. FRX-L data were subjected to a series of checks before the model was used for analysis.

Several tests based on model assumptions were devised to obtain a set of shots and times for analysis. The primary questions are:

- (1) Is radial pressure balance satisfied?
- (2) Is the FRC in equilibrium?
- (3) Is the FRC axisymmetric?
- (4) Are Ohmic dissipation and power losses much smaller than the compressional work done on the FRC?
- (5) Is bulk FRC translation occurring?
- (6) Is the FRC in a decaying equilibrium?

The tests were conducted using an Abel-inverted density profile obtained from multichord interferometry. The inversion used a least-squares regression tomography technique<sup>15</sup> which smooths the density profile on a variable adaptive spatial mesh with polynomial trial functions. This technique was necessary to optimize the execution of a second spatial derivative of density, which was required for one of the tests. A typical density profile is shown in Fig. 6.

To address the first point, we would like to compare the interferometer-derived radius at maximum density and the magnetics-derived radius  $R$  given by  $r_s/\sqrt{2}$ . If radial pressure is balanced in the FRC, the radii should agree within the measurement error. The second and third points are addressed by testing for low  $m$  and  $n$  global MHD modes. This is accomplished by comparing the average density obtained from the central interferometer chord ( $\int n_e dl / 2r_s$ ) with the density obtained by numerically integrating the radial density profile. If the two methods of determining density agree, then we can conclude that the FRC is axisymmetric and unperturbed by MHD modes.

The Ohmic heating was estimated from the radial density profile to test the small perturbation assumption. If the Ohmic heating estimate and the heating value from the

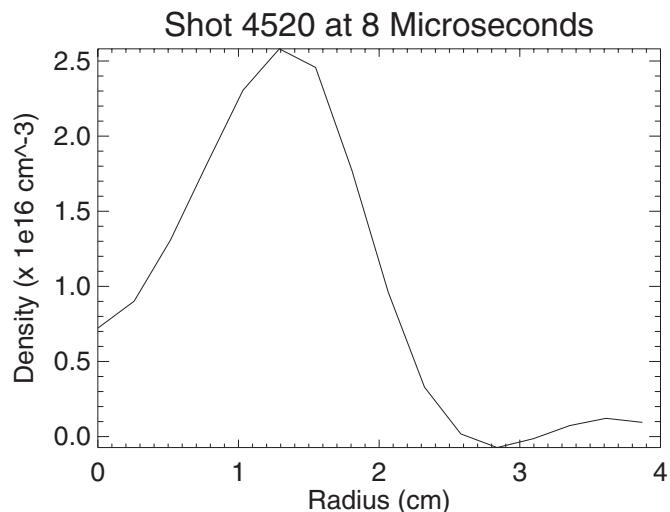


FIG. 6. Shot 4520 density at 8  $\mu\text{s}$  after main bank firing. Example of the least-squares regression method applied to Abel inversion of interferometer data.

model were within measurement error, it was concluded that the model's value of Ohmic heating was acceptable. The fifth point (translation of the FRC) was addressed by assuming the frozen-in flux condition of ideal MHD. If flux is frozen, any bulk motion of the FRC will drag flux with it. This modifies the FRC separatrix profile to show an axial shift in the peak  $r_s$  with time, when the FRC translates.

The final point was satisfied by requiring the input compression power of Fig. 5 to be positive, representing power transferred to the plasma. This was necessary to maintain the "shrinking FRC" equilibrium that the model expects. The result of satisfying the conditions previously listed is the generation of shots and time windows for application of the model to the FRX-L data.

## IV. EXPERIMENTAL RESULTS

Power balance analyses indicate that radiation is an insignificant loss mechanism for FRX-L, and probably high-density FRCs in general. A wider comparison of data than available in the work by Zhang<sup>2</sup> shows that FRX-L plasmas are consistent with the  $\tau_N \approx \tau_\phi$  scaling prevalent in low-density FRC data. Data from the model suggest that trapping more flux during the formation phase of the FRC increases Ohmic heating of the plasma.

### A. Comparison of radiation with other loss mechanisms

Radiated power was insignificant in the majority of shots analyzed for FRX-L. All shots analyzed except one produced FRCs where radiation was less than 5% of the total loss. Most of the data indicate  $P_{\text{rad}} < 1\%$  of the total loss. This is in contrast to the typical result of  $>5\%$  obtained on low-density experiments,<sup>10</sup> including STP-L<sup>16</sup> and FRX-C.<sup>17,4</sup> Using the same zero-dimensional model that was utilized for FRX-L, radiation was found to represent 10%–40% of the total losses for typical shots on LSX.<sup>5</sup>

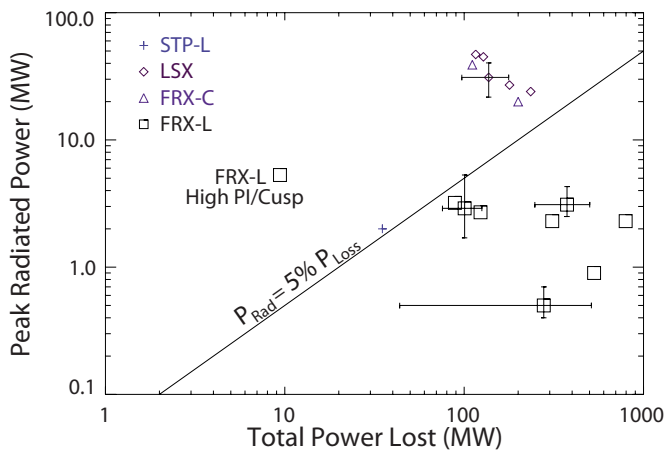


FIG. 7. (Color online) Radiated power vs total loss. Total losses here represent the sum of thermal, particle, and radiative losses from the FRC. Most data show FRX-L radiative losses smaller than 5%, the lower bound of low-density FRCs. The high PI/Cusp shot shows a percentage of radiation loss higher than all previous experiments.

### 1. FRX-L radiated power scales with total plasma power loss

Figure 7 shows the peak radiation for FRX-L shots compared to the total power loss.

This figure also includes data from FRX-C and LSX,<sup>4,17,5</sup> both of which are typical low-density ( $n \leq 10^{21} \text{ m}^{-3}$ ) FRCs. Data have also been included for the  $n_e \approx 4 \times 10^{21} \text{ m}^{-3}$  STP-L plasma.<sup>16</sup> Note that FRX-L has a lower percentage of radiated losses for the same magnitude of power loss as LSX and FRX-C. Assuming that radiation is primarily due to impurities, one can conclude that FRX-L is a much cleaner plasma than previous FRCs.

Figure 8 shows a specific example of a low PI and high cusp shot where the radiation was less than 1% of total losses. The typical shot on FRX-L indicates that radiation is a negligible loss mechanism for high-density FRCs. The only data from the high PI/Cusp shot series show a much higher radiated loss percentage; this is explained in the following paragraphs.

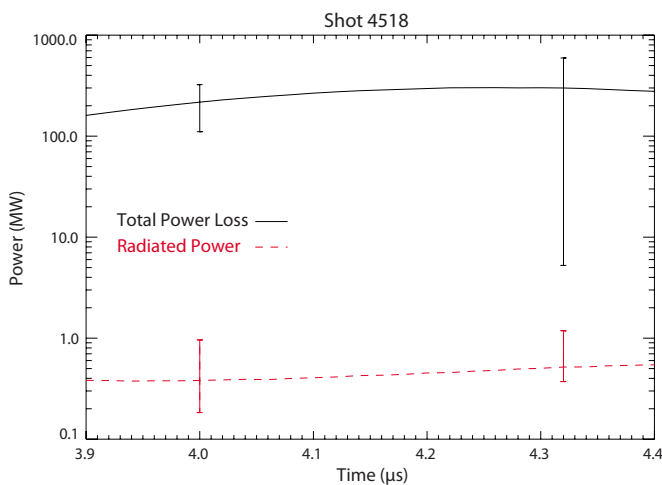


FIG. 8. (Color online) Shot 4518 radiated power. Typical radiation is  $\ll 1\%$  of total loss. Time is measured after the main bank fires.

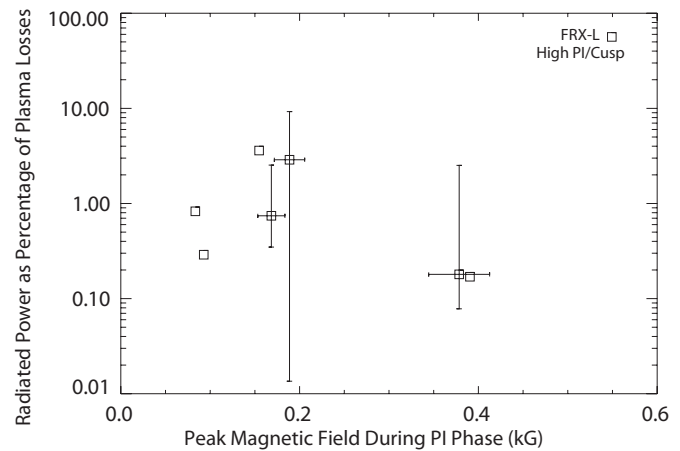


FIG. 9. Dependence of equilibrium FRC radiated power on PI magnitude. The first PI peak in magnetic field after firing shows an increasing trend with the radiated power percentage of total losses. Magnetics values are the average of eight magnetic pickup loops along the length of the theta coil.

When the cusp and PI bank charge voltages were both increased by  $\sim 2$  kV, the radiated power became significant. Figure 7 indicates that one shot (4649) had radiation above the 5% lower bound of low-density experiments; this was the only high cusp and PI shot that was analyzed. The radiated power for this shot is approximately 50% of the total loss, the remainder of which is represented by thermal conduction. This is not entirely surprising, considering the high cusp and PI series of shots was designed to increase radiation loss to significant levels.

The peak magnetic field immediately after the PI bank is fired contributes greatly to the impurities introduced into the plasma, and increases radiation by impurities as a result. Figure 9 shows that the dependence of radiated power as a percentage of the plasma loss shows an increasing trend with respect to the first peak of the PI magnetic field. Note that this figure does not reference the main bank magnetic field.

This effect can be quantified by observing the peak of the external magnetic field after the first “zero” crossing (see Fig. 2). When magnetic field is above zero, the FRC reversal surface moves outside the quartz tube. As the PI peaks higher above zero, more field is put across the wall and more impurities are introduced. Figure 10 shows a comparison between external magnetic fields for a high PI and cusp shot (solid black trace) and a high PI, low cusp shot (dashed red trace). A larger PI peak is produced by a larger cusp magnetic field, which tends to add to the PI field in the theta coil region. The difference in peaks is only 0.4 kG, but this is sufficient to increase impurities substantially.

Further evidence that peak magnetic field after the first PI crossing affects impurity radiation is provided by data from an optical multichannel analyzer (OMA). The OMA has an adjustable grating that gives a view of plasma wavelengths approximately 100 nm wide. The grating was adjusted so that the deuterium beta line (486.0 nm) was viewable in the same window as an oxygen-II cluster of impurity lines ( $\sim 464$  nm). The ratio of the two peaks is a qualitative measure of the impurity level in the plasma, since oxygen is one of the primary impurities inducted from the quartz wall.

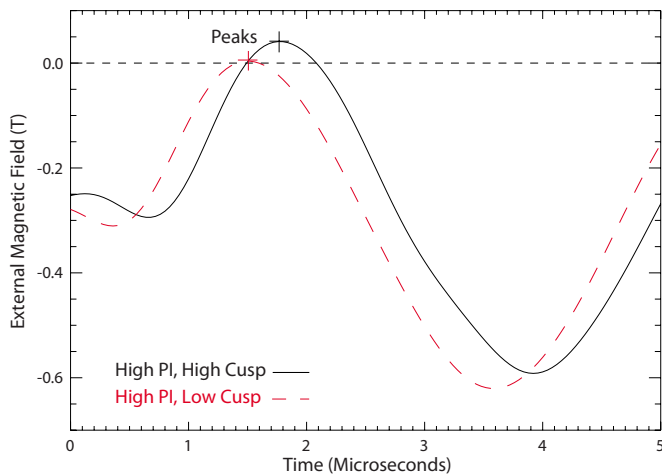


FIG. 10. (Color online) Comparison of PI phases for high and low cusp settings. A higher cusp field causes a “harder” crossing, introducing more plasma impurities from the wall. The difference in peaks is approximately 0.04 T.

The results are shown in Fig. 11. The impurity ratio was plotted to normalize the effect of fill pressure and variations in the spectrometer slit width from shot to shot. Figure 11 clearly shows that the ratio of doubly ionized oxygen to deuterium increases with PI field. This is further evidence for the contention that PI field increases impurities from the wall during the preionization phase.

## 2. Possible explanation of reduced radiative loss in the FRX-L plasma

We observed in the previous section that the percentage of radiation power loss relative to the total power loss was reduced almost an order of magnitude compared to previous low-density FRCs. There is a strong possible reason for this observation, which is postulated in the following paragraph.

The reduction in radiated power may be due to increased plasma density. Assuming that impurities enter the plasma through the scrape-off layer, higher density would lead to a shorter mean free path before ionization. Impurities would

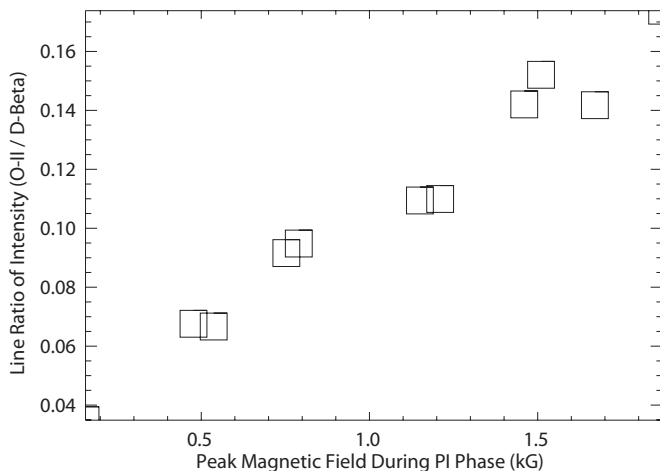


FIG. 11. Dependence of impurities on PI magnetic field. The oxygen impurity ratio shows an increasing dependence on the first PI peak in magnetic field after firing.

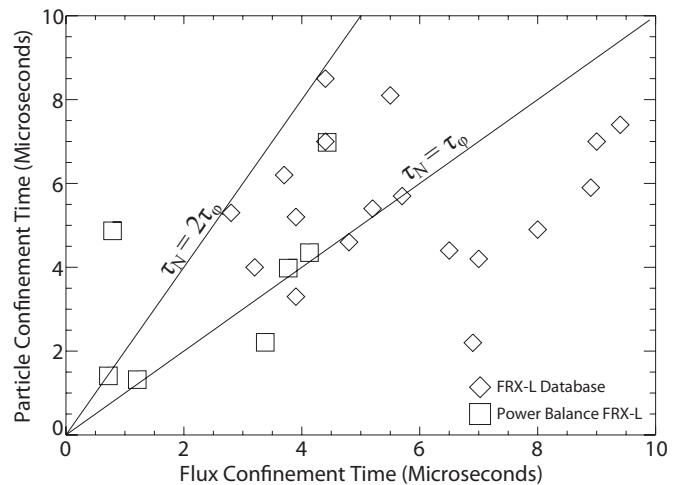


FIG. 12. Comparison of particle and flux lifetimes for FRX-L data. Particle lifetime is approximately equal to flux lifetime in FRX-L; typical low-density FRCs have  $\tau_N/\tau_\phi \lesssim 1$ . Diamonds represent data from old FRX-L campaigns.

therefore ionize before penetrating the core plasma, and the plasma would be shielded by edge effects. It is interesting to note that, in tokamak configurations, regression fitting of available data indicates that  $Z_{\text{eff}}$  is inversely proportional to the square of density.<sup>18</sup>

## B. FRX-L particle and flux lifetime scaling similar to previous low-density FRCs

Previous low-density experiments have shown that particle and flux lifetimes are approximately equal.<sup>8,19</sup> We also observe that  $\tau_N \approx \tau_\phi$  for FRX-L. This trend is apparent when we consider data from older (pre-2006) campaigns, as well as data used for the power balance study. Figure 12 shows measured flux and particle confinement times. When constrained to intersect the origin, a linear regression of the data gives a slope of 1.0. Thus, although there is a great deal of scatter present, the best fit to the data is consistent with the  $\tau_N \approx \tau_\phi$  scaling. It is useful to show that we follow low-density lifetime comparative scaling, which allows us to extrapolate to two orders of magnitude higher density to the compressed FRC for MTF.

An earlier paper<sup>2</sup> showed that  $\tau_N \approx 2\tau_\phi$  for a selection of approximately 10 shots. In the cited paper,  $\tau_N$  and  $\tau_\phi$  were determined from a 4  $\mu\text{s}$  subset of the available data. For the data in Fig. 12,  $\tau_N$  and  $\tau_\phi$  were obtained by analyzing flux and particle histories from just after FRC formation until the separatrix collapsed ( $r_s \approx 0$ ). An extended time history was necessary to observe the FRC for at least one e-folding time and verify the confinement time estimate. Additional data show that the average behavior of confinement on FRX-L is  $\tau_N \approx \tau_\phi$ .

## C. Trapped poloidal flux increases Ohmic heating

Fusion-relevant FRC plasmas need higher temperature than available after the initial shocked formation of the plasma. According to semiempirical scaling,<sup>20,21</sup> plasma heating should correlate with the  $G_{LO}$  factor, which is a mea-

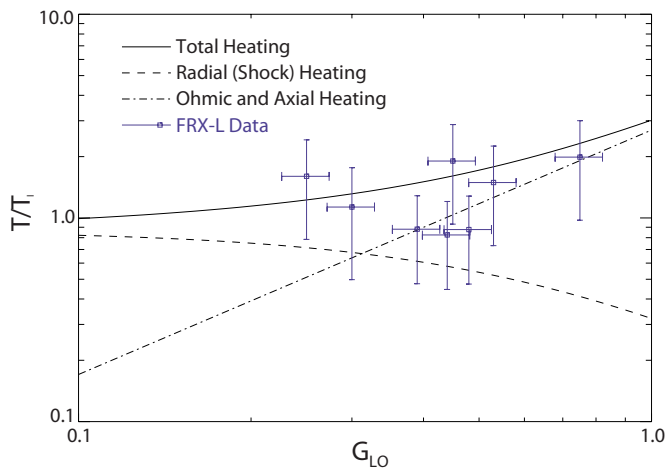


FIG. 13. (Color online) FRC heating compared to experimentally determined  $G_{LO}$ . FRX-L data follow empirical data from low-density FRCs to heating related to  $G_{LO}$ .  $G_{LO}$  is heavily influenced by initial trapped flux.

sure of the maximum external flux that can be trapped in the FRC. In order to apply FRC scaling laws to the high density compressed MTF regime, it is necessary to determine if FRX-L follows the  $G_{LO}$  scaling which was developed using data from low-density FRCs.  $G_{LO}$  scaling shows that temperature can become fusion-relevant after initial FRC formation without particle injection or other external heating methods.

$G_{LO}$  scaling predicts a correlation between flux trapped at FRC formation and plasma heating.  $G_{LO}$  is a measure of the efficiency of flux-trapping;  $G_{LO}=1.0$  would represent maximum theoretical flux-trapping in a shock-formed theta pinch. A semiempirical model for FRC formation using the rigid rotor is summarized by Tuszewski.<sup>20</sup> Figure 13 shows that FRX-L shots approximately follow this model. One should note that  $T/T_i$  on the y-axis in the figure represents the ratio of the temperature at FRC equilibrium to that when bias field is zero. FRX-L shots are above the pure shock heating curve and show an increasing trend with  $G_{LO}$  just as the semiempirical model does. Most shots fall below the total heating curve, however, which indicates that the model may be too optimistic for temperature predictions. The trend of increasing  $T/T_i$  with  $G_{LO}$  is reinforced by the FRX-L data however.

In support of this result, the power balance analysis of FRX-L data demonstrates that dissipation of the flux trapped in the FRC heats the plasma by Ohmic dissipation. The flux for various FRX-L shots was taken at  $1.5 \mu\text{s}$  after the FRC equilibrium is achieved. Figure 14 shows that trapped flux and Ohmic heating are directly correlated.

Since FRX-L data approximately follow the  $G_{LO}$  scaling, we can conclude that higher plasma temperature is achievable by trapping more flux. This is accomplished by increasing the magnetic field at lift-off time ( $B_{LO}$ ) with the Green-Newton field held constant, i.e., more to the right on the  $G_{LO}$  axis. Green-Newton field only depends on the charge voltage of the main bank and fill pressure, which can be controlled. Larger  $B_{LO}$  should thus lead to greater Ohmic heating and higher final temperatures.

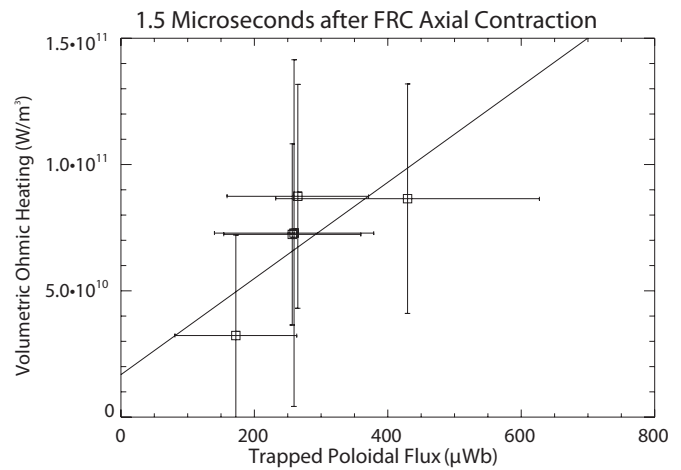


FIG. 14. Ohmic heating vs trapped flux. There is a distinguishable increasing trend when volumetric Ohmic heating ( $P_{\text{Ohmic}}/V_{\text{FRC}}$ ) is compared to trapped flux; values are taken  $1.5 \mu\text{s}$  after FRC axial contraction. Sigma weighting is used for the linear regression to provide the most probable fit.

## V. SUMMARY

A global power balance analysis has been performed for FRX-L FRCs with typical parameters  $\langle n \rangle \approx 1-5 \times 10^{16} \text{ cm}^{-3}$ ,  $T_{\text{tot}} \approx 200-300 \text{ eV}$ , and lifetimes of approximately  $10 \mu\text{s}$ . The key findings are as follows: first, the percentage of radiative losses relative to total loss is between 1% and 5%. Second, Ohmic heating was found to correlate with the poloidal flux trapping at FRC formation. Third, high density FRCs analyzed in this work reinforce low-density adiabatic scaling which shows that flux and particle confinement times are approximately equal.

All FRCs analyzed, save one, produced the result that radiation is an insignificant source of loss for these high-density FRCs when compared to particle loss and thermal conduction. The one setting of “high” cusp and PI fields produced large relative radiation losses due to increased ablation of impurities from the silicate vessel wall. This scenario can easily be avoided in future FRX-L studies. The result that radiated power is negligible compared to the total loss for FRX-L suggests that high density FRCs can be favorable for reducing the relative radiation power loss. This is another benefit of scaling FRCs to higher density, particularly for MTF.

A semiempirical  $G_{LO}$  scaling<sup>20</sup> predicted by data from FRX-C and TRX-2 was compared to the FRX-L data. The data from FRX-L show the same general increasing trend of the scaling model. Volumetric Ohmic heating also showed an increasing trend with the flux trapped for these high density FRCs. This is expected because the dissipation of trapped poloidal flux inside the FRC separatrix should be the primary source of heating after formation. FRX-L data lend support to this hypothesis. Based on this result, FRX-L can increase heating for the FRC-MTF target by trapping more flux at FRC formation. A method of accomplishing this would be to increase the bias field.

Particle and flux confinement times on FRX-L were believed to differ by as much as a factor of 2 in a previous study.<sup>2</sup> By analyzing the flux and particle histories for longer

periods of time than in the previous study, a wider spread of confinement times was obtained. This was necessary in the present study in order to observe the evolution of these quantities for at least one e-folding time. The spread of confinement times measured on FRX-L shows that the average behavior is the same as seen in low-density FRC experiments, i.e.,  $\tau_N \approx \tau_\phi$ . Confinement time scaling from adiabatic considerations<sup>10</sup> should be applicable to high-density FRCs, although other scalings were not tested. Low-density scaling should extend beyond FRX-L to the higher density regime of a compressed FRC target for MTF.

## ACKNOWLEDGMENTS

This work was supported by the Office of Fusion Energy Sciences at Los Alamos National Laboratory, U.S. Department of Energy under Contract No. DE-AC52-06NA25396.

<sup>1</sup>R. C. Kirkpatrick, I. R. Lindemuth, and M. S. Ward, *Fusion Technol.* **27**, 201 (1995).

<sup>2</sup>S. Zhang, T. P. Intrator, G. A. Wurden, W. J. Waganaar, J. M. Taccetti, R. Renneke, C. Grabowski, and E. L. Ruden, *Phys. Plasmas* **12**, 052513 (2005).

<sup>3</sup>J. H. Degnan, D. Amdahl, A. Brown, T. Cavazos, S. K. Coffey, G. G. Craddock, M. H. Frese, S. D. Frese, D. Gale, T. C. Grabowski, G. F. Kiuttu, F. M. Lehr, J. D. Letterio, J. Peterkin, R. E. N. F. Roderick, E. L. Ruden, R. E. Siemon, W. Sommars, and P. J. Turchi, in *31st IEEE International Conference on Plasma Science, 28 June–1 July 2004, Baltimore, MD, USA* (IEEE, Piscataway, NJ, 2004), p. 161, conference publication copyright 2005 IEE.

<sup>4</sup>D. J. Rej and M. Tuszewski, *Phys. Fluids* **27**, 1514 (1984).

<sup>5</sup>R. J. Maqueda, Ph.D. thesis, University of Washington, 1993.

<sup>6</sup>R. Raman, G. C. Vlases, and T. R. Jarboe, *Nucl. Fusion* **33**, 1685 (1993).

<sup>7</sup>W. T. Armstrong, R. K. Linford, J. Lipson, D. A. Platts, and E. G. Sherwood, *Phys. Fluids* **24**, 2068 (1981).

<sup>8</sup>J. T. Slough, A. L. Hoffman, R. D. Milroy, D. G. Harding, and L. C. Steinhauer, *Nucl. Fusion* **24**, 1537 (1984).

<sup>9</sup>H. Y. Guo and A. L. Hoffman, *Phys. Plasmas* **11**, 1087 (2004).

<sup>10</sup>M. Tuszewski, *Nucl. Fusion* **28**, 2033 (1988).

<sup>11</sup>J. M. Taccetti, T. P. Intrator, G. A. Wurden, S. Y. Zhang, R. Aragon, P. N. Assmus, C. M. Bass, C. Carey, S. A. deVries, W. J. Fienup, I. Furno, S. C. Hsu, M. P. Kozar, M. C. Langner, J. Liang, R. J. Maqueda, R. A. Martinez, P. G. Sanchez, K. F. Schoenberg, K. J. Scott, R. E. Siemon, E. M. Tejero, E. H. Trask, M. Tuszewski, W. J. Waganaar, C. Grabowski, E. L. Ruden, J. H. Degnan, T. Cavazos, D. G. Gale, and W. Sommars, *Rev. Sci. Instrum.* **74**, 4314 (2003).

<sup>12</sup>E. L. Ruden, S. Y. Zhang, T. P. Intrator, and G. A. Wurden, *Phys. Plasmas* **13**, 122505 (2006).

<sup>13</sup>R. J. Maqueda, G. A. Wurden, and E. A. Crawford, *Rev. Sci. Instrum.* **63**, 4717 (1992).

<sup>14</sup>R. L. Spencer, M. Tuszewski, and R. K. Linford, *Phys. Fluids* **26**, 1564 (1983).

<sup>15</sup>E. L. Ruden, S. Zhang, G. A. Wurden, T. P. Intrator, R. Renneke, W. J. Waganaar, F. T. Analla, and T. C. Grabowski, *Rev. Sci. Instrum.* **77**, 103502 (2006).

<sup>16</sup>Y. Aso, S. Himeno, and K. Hirano, *Nucl. Fusion* **23**, 751 (1983).

<sup>17</sup>R. E. Siemon, W. T. Armstrong, D. C. Barnes, R. R. Bartsch, R. E. Chrien, J. C. Cochrane, W. N. Hugrass, R. W. Kewish, P. L. Klingner, H. R. Lewis, R. K. Linford, K. F. McKenna, R. D. Milroy, D. J. Rej, J. L. Schwarzmeier, C. E. Seyler, E. G. Sherwood, R. L. Spencer, and M. Tuszewski, *Fusion Technol.* **9**, 13 (1986).

<sup>18</sup>G. F. Matthews, S. Allen, N. Asakura, J. Goetz, H. Guo, A. Kallenbach, B. Lipschultz, K. McCormick, M. Stamp, U. Samm, P. C. Stangeby, K.-H. Steuer, A. Taroni, B. Unterberg, and P. West, *J. Nucl. Mater.* **241–243**, 450 (1997).

<sup>19</sup>L. C. Steinhauer, *Phys. Fluids* **28**, 3333 (1985).

<sup>20</sup>M. Tuszewski, *Phys. Fluids* **31**, 3754 (1988).

<sup>21</sup>A. L. Hoffman, R. D. Milroy, J. T. Slough, and L. C. Steinhauer, *Fusion Technol.* **9**, 48 (1986).